Slip distribution of the February 27, 2010 Mw = 8.8 Maule Earthquake, central Chile, from static and high-rate GPS, InSAR, and broadband teleseismic data

Bertrand Delouis,[1] Jean-Mathieu Nocquet,[1] and Martin Vallée[1]

Received 6 May 2010; revised 16 July 2010; accepted 4 August 2010; published 10 September 2010.

[1] The shallow depth underthrust earthquake of February 27, 2010 (Mw 8.8) ruptured the subduction plate interface in central Chile between 34°S and 38°S. We retrieve the spatial and temporal distribution of slip during this mega-earthquake through a joint inversion of teleseismic records, InSAR and High Rate GPS (HRGPS) data. Additionally, our model is shown to agree with broadband surface waves. Rupture initiated at about 32 km depth and propagated bilaterally resulting in two main slip zones located SSW and NNE of the hypocenter. Nucleation did not take place within or at the edge of one of these main asperities, but in between. During the first 30s, slip propagated predominantly southwards. Later on, the rupture evolved more slowly and more symmetrically. Eventually, the northern asperity became predominant with maximum slip reaching about 20 m. Most of the seismic moment was released within 110s, a relatively short time, explained by the bilateral propagation. The overall average rupture velocity is 2.6 km/s but propagation occurred initially faster towards the south (3.2 km/s). Large slip did not reach the trench, a result consistent with the moderate size of the tsunami. Down-dip, rupture stopped at about 50 km depth, in agreement with the lower limit of the locked zone inferred by Ruegg et al. (2009) from pre-seismic GPS data. **Citation:** Delouis, B., J.-M. Nocquet, and M. Vallée (2010), Slip distribution of the February 27, 2010 Mw = 8.8 Maule Earthquake, central Chile, from static and high-rate GPS, InSAR, and broadband teleseismic data, *Geophys. Res. Lett.*, *37*, L17305, doi:10.1029/2010GL043899.

1. Introduction

[2] Central Chile, in the vicinity of the cities of Concepción and Constitución, was struck by a major earthquake on February 27, 2010. The capital of Santiago de Chile was also strongly shaken by this event. Rapid source determinations from USGS (http://earthquake.usgs.gov/earthquakes/eqinthenews/2010/us2010tfan/#scitech), GCMT (http://www.globalcmt.org/), recently developed SCARDEC method (http://geoazur.oca.eu/spip.php?article675) all established the underthrust mechanism and moment magnitude (Mw) of 8.8. With a shallow depth (< 50 km) and a nodal plane dipping with a low angle to the East, it could be quickly categorized as an interplate subduction earthquake, at the interface between the subducting Nazca and overriding South-American plates. This was also immediately confirmed by the tsunami generated. Moreover, the subduction segment located between 35°S and 37°S had been shown to be strongly coupled [*Ruegg et al.*, 2009; *Madariaga et al.*, 2010] with a large slip deficit accumulated since the 1835 earthquake.

[3] Rapid slip during large earthquakes triggers seismic waves in the near, intermediate, and far fields that are detected on the Earth surface and that can be used to infer the characteristics of the rupture history. Geodetic data, by quantifying the static displacement on the Earth's surface resulting from the combination of the intermediate and near field terms, enable us to recover the spatial distribution of slip, but are insensitive to the time evolution of slip during the rupture. Seismological data are sensitive to both the spatial and temporal properties of the rupture, but trade-off between parameters describing the spatial and temporal distribution of slip can hardly be avoided without static constraints. Therefore, the most precise descriptions of the rupture history can be provided by joint inversions of seismological and geodetic data.

[4] In this study, we present a joint inversion of the Mw = 8.8, February 27, 2010 Chile earthquake rupture using static and 1Hz kinematic GPS, teleseismic, and InSAR data. High Rate GPS (HRGPS) records offer the advantage to directly record the position time evolution (instead of velocity or acceleration), and never saturate even in case of large and rapid motion, making this data particularly useful at short or regional distances. Such a comprehensive set of data enables us to reliably determine the main characteristics of the slip distribution of the mainshock, with only very minor contamination from possible post-seismic deformation.

2. Data

2.1. Static GPS Data

[5] We use the GAMIT/GLOBK software package v10.35 [*Herring et al.*, 2009] to process two sub-networks of 40 continuous GPS (CGPS) stations over South America provided by the International GNSS Service (IGS) [*Dow et al.*, 2009] and the Red Argentina de Monitoreo Satelital Continuo (RAMSAC, http://www.ign.gob.ar/ramsac). We first derive daily time series by combining the two sub-networks into a single position solution expressed with respect to the International Reference Frame 2005 (ITRF2005) [*Altamimi et al.*, 2007]. We carefully checked that the 18 sites used to define the frame were not impacted by the co-seismic displacement. Co-seismic displacements were estimated using an average of 7 days before the earthquake and the day following the earthquake to avoid any contamination of

[1]Geoazur, Observatoire de la Côte d'Azur, Université de Nice – Sophia Antipolis, CNRS, IRD, Valbonne, France.

0094-8276/10/2010GL043899

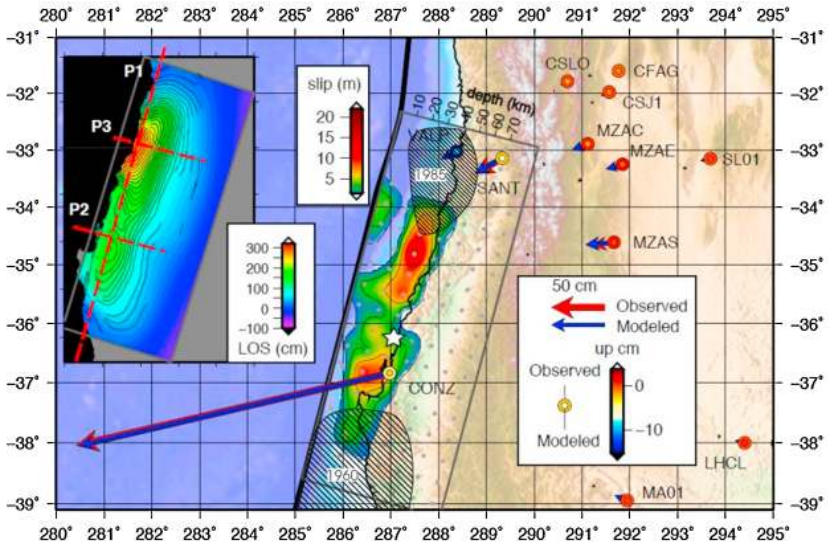

Figure 1. Location of the rupture model (gray rectangle) and slip distribution projected onto the Earth surface. Gray dots indicate the center of subfaults or points sources used to discretize the fault model. Heavy black line: trench; Red and blue arrows: observed and computed horizontal displacement from GPS, respectively. Bicolor circles: observed (outer ring) and computed (inner part) vertical displacement for GPS static data, respectively. Insert: unwrapped InSAR data (raw data © JAXA and METI, interferogram processed by NIED, see text for more details). Red dashed lines correspond to the three profiles shown in Figure 2a. The location of the cities of Concepción, Santiago, and Valparaiso is indicated by GPS stations CONZ, SANT, and VALP respectively. Hatched surfaces correspond to the rupture surfaces of the 1960 south Chile - Valdivia and 1985 central Chile – Valparaiso earthquakes. The 1960 rupture area is from *Plafker and Savage* [1970] and *Ruegg et al.* [2009], and the 1985 rupture zone is redrawn to combine the slip distribution obtained by *Mendoza et al.* [1994] and the aftershock area from *Barrientos* [1995].

the co-seismic displacement estimates by rapid post-seismic motion. The co-seismic displacement is determined with a precision better than one cm on the horizontal components and 2 cm on the vertical component. Figure 1 shows the GPS stations and their horizontal and vertical co-seismic displacements used in the inversion (auxiliary material Table S1).[1]

2.2. High Rate GPS Data

[6] For a subset of the CGPS sites, we processed 1 Hz data for a time window of one hour including the time of the earthquake using a two steps approach. First, single differences are formed to derive the Doppler shift (the rate of phase difference between two epochs of measurements) and we invert for the position change with respect to the first epoch of measurements. The obtained time series are used to determine the arrival time of the first seismic waves. We use this information to select a subset of reference sites in the far field (>800 km) that can be considered as fixed during the first 400 s following the earthquake. For each site in the near field, we used the track software [*Herring et al.*, 2009] which uses double-difference carrier phase to solve for the phase ambiguities and the 3D position at each epoch. We keep the same selection of satellite during the full time window to improve stability of the solution. We carefully check phase residuals for each satellite and remove GPS satellites PRN 17 & 4 because of their large systematic residuals. We chose RIO2 (longitude E292.25°, latitude −53.7855°) as the reference site providing the best stability of the result.

[7] We applied a sideral filtering [*Choi et al.*, 2004] using the time series from the day before the earthquake. Sideral filtering significantly reduces the long period drift (>100s). The static displacement obtained from the kinematic processing agree within 2 cm with the one derived from the GAMIT/GLOBK static processing, indicating very little rapid post-seismic deformation occurring hours after the earthquake. Depending on the quality of the displacement time series obtained, HRGPS records were high-pass filtered with a cut frequency varying between 0.005 and 0.02 Hz, and low-pass filtered at 0.03 Hz. As a result, the inversion is performed at low frequency, in a range appropriate to recover the main characteristics of the rupture process for such a mega-earthquake (Mw 8.8).

2.3. InSAR Data

[8] We use a Synthetic Aperture Radar (SAR) interferogram covering the essential part of the rupture zone of the February 27, 2010 earthquake. It was produced by NIED [*Ozawa*, 2010] from ALOS/PALSAR ScanSAR raw data of METI and JAXA (Ministry of Economy, Trade and Industry of Japan, and Japan Aerospace Exploration Agency). The InSAR image was released at http://supersites.unavco.org/chile.php. It corresponds to the descending path 422 of ALOS, with master 2008/04/10 and slave 2010/03/01. In the inversion, we incorporated 1172 points distributed along the fringes reproduced in Figure 1. Unwrapping of the InSAR data was performed using the static displacement at GPS station CONZ as a calibration point and inverting for a line of sight (LOS) offset.

[1]Auxiliary materials are available in the HTML. doi:10.1029/2010GL043899.

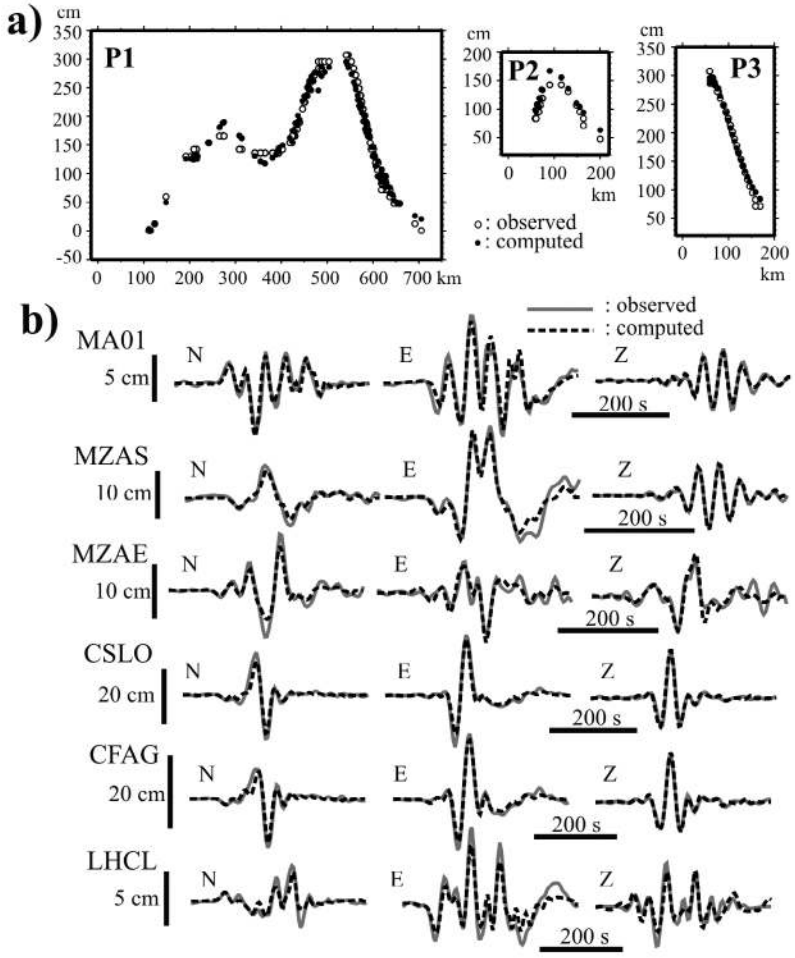

Figure 2. (a) Three profiles (P1, P2, P3) across the SAR interferogram to illustrate data fitting. LOS: Line Of Sight displacement (positive means increasing of the satellite-to-ground distance). Horizontal axes: distance with respect to an arbitrary origin. (b) Modeling of the HRGPS records. Station locations are shown in Figure 1.

2.4. Teleseismic Broadband Data

[9] Teleseismic waveforms of the FDSN (Federation of Digital Seismograph Networks) were retrieved from the IRIS data center (http://www.iris.edu/wilber) for 24 broadband stations located at distances comprised between 45° and 78° and sampling the range of available azimuths. Processing of the teleseismic records includes deconvolution from the instrument response, integration to obtain displacement, windowing around the P (vertical) and SH (horizontal transverse) wave trains, equalization to a common magnification and epicentral distance, bandpass filtering between 0.01 and 0.8 Hz for the P waves and 0.01 to 0.4 Hz for the S waves.

3. Inversion Procedure

[10] We first determined the focal mechanism of the February 27, 2010 earthquake by modeling the teleseismic waveforms. We performed a series of joint inversions and found that (strike, dip, rake) = (15, 18, 110) provides the best fit to the seismological and geodetic datasets. Our estimate is almost identical to the GCMT and USGS-CMT solutions, (strike, dip, rake) = (18, 18, 112) and (14, 19, 104) respectively.

[11] Our kinematic modeling follows the approach described by *Delouis et al.* [2002]. The model consists of a single fault segment, 720 km long and 280 km wide, subdivided into 126 subfaults measuring 40 km along strike and dip, evenly distributed on the fault plane. The model area is purposely taken larger than the expected rupture surface in order to discriminate clearly the areas which slipped from those which did not. The strike and dip angles of the fault are kept fixed: (strike, dip) = (15°, 18°). Rupture initiation, i.e. the model hypocenter, is located at 36.208°S, 72.963°W, provided by the DGF (Departamento de Geofisica, Universidad de Chile, http://www.dgf.uchile.cl) and at a depth of 32 km. Although DGF's epicenter is located 40 km to the SSW of the estimate from NEIC/USGS epicenter, this location was found to provide the optimal fit to the combined datasets, compared to NEIC/USGS epicenter and intermediate locations.

[12] To model the waveforms, the continuous rupture is approximated by a summation of point sources, one at the center of each subfault. To model the static displacements, subfaults are represented by dislocation surfaces. For each point source, a local source time function is defined, corresponding to the rate of seismic moment locally released. It is represented by three mutually overlapping

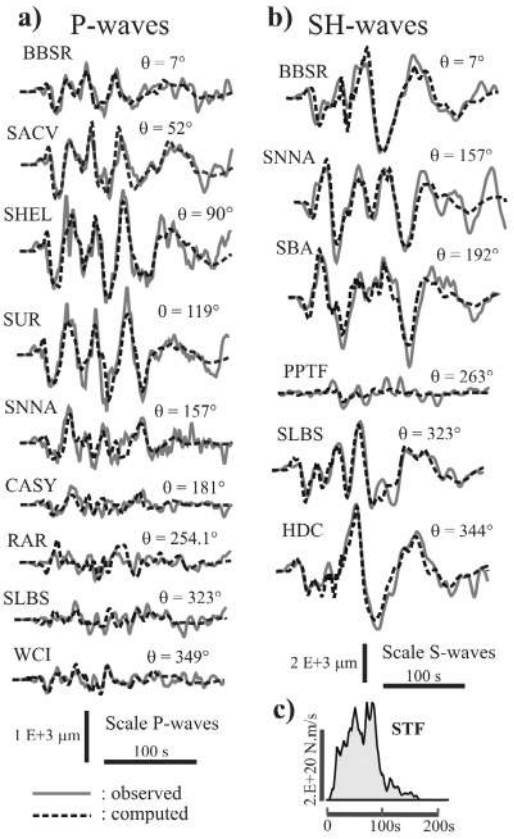

Figure 3. Modeling of the teleseismic records, for the (a) P-waves and (b) SH-waves. Amplitudes have been normalized to a common epicentral distance. Only a subset of data is displayed, the complete set of records is shown in the auxiliary material. (c) The overall source time function (STF). In Figures 2a and 2b θ is the azimuth of the station.

isosceles triangular functions of duration equal to 12s, allowing the local source time function to last for a maximum of 24s. For each of the 126 subfaults (points sources), the parameters to be inverted for are the slip onset time, the rake angle, and the amplitudes of the three triangular functions. Rupture onset times are bounded according to a minimum and a maximum rupture velocity of 1.8 and 3.5 km/s. The rake angle can vary between 100° and 120°.

[13] A non-linear inversion is performed using a simulated annealing optimization algorithm. Convergence criterion is based on the simultaneous minimization of the root mean square (rms) data misfit and of the total seismic moment. The rms misfit error is the average of the normalized rms errors of the individual data sets (teleseismic, InSAR, static GPS, and HRGPS), equally weighted. Minimization of the total seismic moment is required to reduce spurious slip in the fault model. We also verified that the main features of the slip model described below are stable when the relative weights of the individual datasets are modified by as much as 50%.

[14] Synthetic seismograms at local to regional distances (HRGPS data) are computed using the discrete wave number method of *Bouchon* [1981] designed for one-dimensional velocity models. Synthetic seismograms at teleseismic stations were generated using ray-theory approximation and the approach by *Nabelek* [1984]. We used the CRUST2.0 global crustal velocity model from Laske, Masters, and Reif (http://igppweb.ucsd.edu/~gabi/rem.html) in the epicentral area. Static displacements (for static GPS and InSAR) are computed using the dislocation formulation of *Savage* [1980] at the surface of a semi-infinite elastic half space.

4. Inversion Results and Resolution

[15] The slip map resulting from the joint inversion is projected onto the Earth surface in Figure 1. It displays two main slip zones, or asperities, located one SSW and the other NNE from the epicenter, therefore demonstrating the bilateral character of rupture propagation. Slip within the hypocentral area is relatively moderate (4 to 8m) while it reaches 13m and 21m at the SSW and NNE asperities respectively. Total rupture length is about 500 km along strike. In the up-dip direction, large slip stops 20–40 km from the trench (except between lat. −34.4° and −33.5°), a feature which certainly limited the size of the induced tsunami. In the down-dip direction, slip stops rather uniformly between 45 and 50 km depth (Figure 1).

[16] Observed versus values predicted by our joint inversion are shown in Figure 1 for the static GPS, in Figure 2 for the InSAR (a) and HRGPS (b), and in Figure 3 for the teleseismic records. The InSAR data, with a clear closure of the fringes in the north and in the south provide strong constraints on the rupture terminations (Figure 1) and display two well marked maxima corresponding to the two major slip zones (see profile P1 in Figure 2a). The HRGPS time series are modeled in the same way as would be strong motion records (Figure 2b). Figure 3 shows waveform modeling of the teleseismic P and SH waves for a subset of stations spanning different azimuths, the complete set of stations being shown in the auxiliary material. The mainshock source time function (STF, Figure 3c) indicates that most of the seismic moment was released during the first 110s. The slip weighted average rupture velocity is 2.6 km/s but on average, propagation was slightly faster towards the south (2.7 km/s) than towards the North (2.5 km/s). The difference is mainly due to the initial part of rupture propagation, which is faster towards the south (3.2 km/s) in the first 30s.

[17] To explore the stability of the solution with the discretization of the fault model, we carried out two additional joint inversions, one with the mesh of subfaults shifted 20 km towards the East, and one with a finer grid spacing, 20 km instead of 40 km. The corresponding slip maps are presented in the auxiliary material. These tests show that the results presented in this paper are stable with respect to reasonable variations of the mesh of subfaults.

[18] Figure 4a introduces a snapshot view of the rupture time evolution, displaying the cumulative slip pattern with six time steps. During the first 45s of rupture, slip developed essentially towards the south. At the same time the along-dip extent of the rupture was almost achieved. Thereafter (see t = 60s), the pattern became more symmetrical. From 75s on, the northern slip zone becomes predominant. Finally, the overall slip pattern is moderately asymmetrical, with 60% of the seismic moment released in the NNE and 40% in the SSW. The total seismic moment is 1.8E + 22 N. m (Mw = 8.8). The slip model is provided in ASCII format in the auxiliary material.

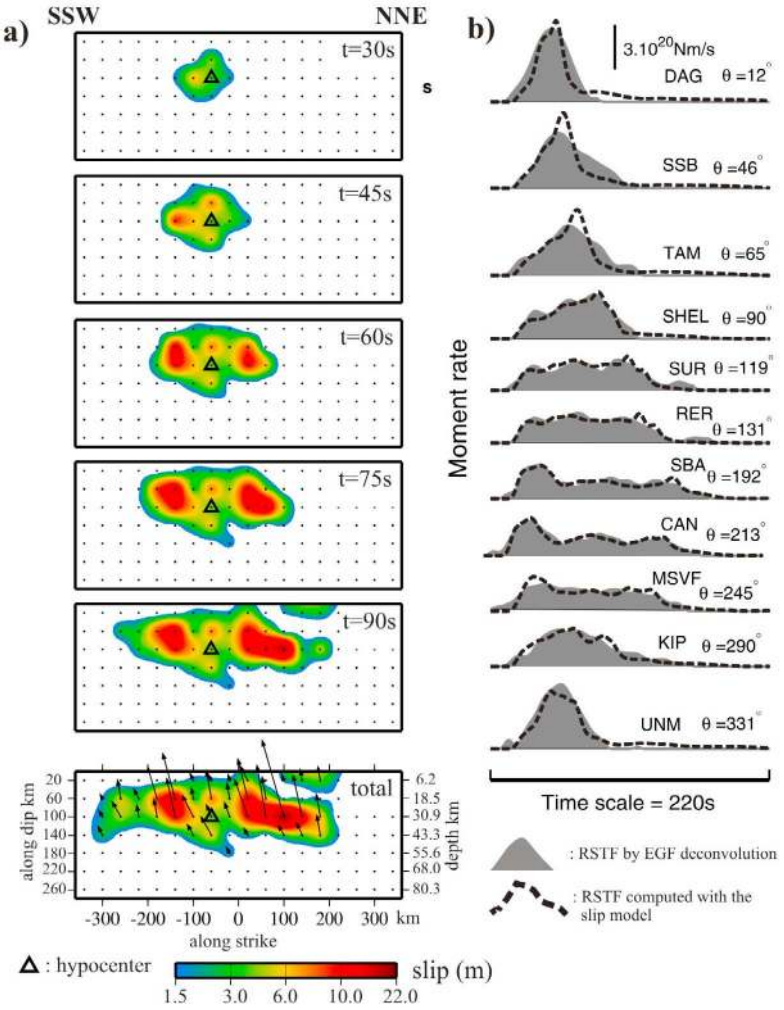

Figure 4. (a) Snapshots of the slip distribution resulting from the joint inversion. Cumulative slip shown in six time steps. The last map (bottom, indicated "total") displays the final slip distribution. Black arrows are the slip vectors. (b) Comparison between observed and computed RSTFs. Observed RSTFs (filled curves) are obtained by stabilized deconvolution of the 2010/03/05 aftershock (Mw = 6.6) transverse signals from the main shock transverse signals, in the Love-wave time window. Computed RSTFs (dashed curves) are computed from our rupture process model. A 10s smoothing is applied to both observed and computed RSTFs. The name and azimuth of the selected FDSN stations, as well as the amplitude scale, are shown. θ is the azimuth of the station.

[19] We further validate our kinematic source model through a comparison with broadband surface waves recorded at teleseismic stations. To do so, we adopt an Empirical Green Function (EGF) approach, using as EGFs two Mw = 6.6 aftershocks (2010/03/05 and 2010/03/16). Theoretically, the Relative Source Time Functions (RSTFs) can be obtained by a direct deconvolution of the EGF signal from the main shock signal [*Hartzell*, 1978]. However, the inherent instability of the deconvolution operator may pollute the results. To retrieve more reliable RSTFs, we apply the stabilized deconvolution technique of *Vallée* [2004], in which four physical constraints on the RSTFs (causality, positivity, limited duration, and equal area) are integrated in the deconvolution process. We verified that the RSTFs are little sensitive on the selected aftershock. Figure 4b shows the Love-waves RSTFs, recorded at 11 stations of the FDSN (filled curves), together with the RSTFs derived from our spatio-temporal model, considering a Love-waves phase velocity equal to 4.5 km/s [*Schwartz*, 1999]. Because variations of the RSTFs as a function of station azimuth are directly related to the rupture process characteristics, the high similarity between observed and computed RSTFs is a strong indicator of the realness of our proposed source model. It confirms two of the main earthquake propagation characteristics: (1) the dominant moment release North of epicenter, as shown by the more compact RSTFs in this direction (stations DAG, SSB, and UNM), and (2) the minor but early southward rupture propagation, as evidenced by the impulsive RSTF initiation at stations SBA and CAN.

[20] Synthetic tests were carried out in order to assess how the resolution of the slip distribution may vary on the fault model and what is the contribution of the different datasets. In addition, we assess the relative power of resolution of the separate and joint inversions. The synthetic model and the inversions are shown in the auxiliary material. The main results from those tests are: i) among the individual datasets,

the InSAR data provides the best constraint on the slip location. This is to be expected given the good coverage of the InSAR data points in the coastal area; ii) the best retrieval of the synthetic asperities is obtained with the joint inversion. This is usually the case, each individual dataset contributing to the overall resolution in the joint inversion; iii) slip in the upper part of the model, i.e. nearest to the trench, is less well resolved. This is related to the lack of measuring points offshore between the coast and the trench.

5. Discussion and Conclusion

[21] Our analysis of the 2010 Chile earthquake is performed at relatively low frequency, our aim being to recover the main and robust characteristics of the slip distribution of this mega earthquake. Further studies using additional data and higher frequencies will certainly provide finer details of the rupture process. However, our joint inversion clearly evidences a bilateral propagation of rupture, extending about 250 km on both sides of the epicenter, the overall slip pattern being moderately asymmetrical, with 20% more seismic moment released in the NNE than in the SSW. Remarkably, the depth of 50 km found for the down-dip end of the rupture agrees with estimates for the down-dip end of the locked zone derived from GPS surface measurements [*Ruegg et al.*, 2009]. It is also identical to that found for large interplate earthquakes in northern Chile [*Delouis et al.*, 1997; *Pritchard and Simons*, 2006; *Delouis et al.*, 2009], suggesting a transition from seismic to aseismic behavior at that depth for a large segment of the south American subduction. Near the trench, despite a lower resolution on the slip distribution, our model clearly shows that large slip did not occur in the uppermost part of the plate interface, a result consistent with the relatively moderate size of the tsunami triggered by such a large earthquake. The rupture timing is constrained by the teleseismic body waves and by the HRGPS records. Both data show that, during the first 30s, the rupture propagated southwards with a velocity faster than the average velocity (2.6 km/s). About 60s after rupture initiation, the slip distribution displays an almost symmetrical pattern on both sides of the hypocenter. After 75s, slip becomes predominant in the North. This time evolution is confirmed independently by the relative source time functions at teleseismic stations obtained from surface waves. The effective duration of rupture is about 110s, a relatively short duration for a Mw 8.8 earthquake, but well explained by the bilateral propagation, causing two areas to release a large amount of moment partially simultaneously. Slip in the epicentral area is relatively small with respect to the major slip zones on both sides. Clearly, the initiation of the 2010 Chile mainshock did not take place within a main asperity.

[22] The northern and southern termination of the rupture are well constrained, especially with the help of the InSAR data. Towards the south, large slip ends at 37.2°S and from there, rapidly decreases near 38°S. This corresponds within the uncertainty to the northern limit of the 1960 M > 9.5 south Chile - Valdivia earthquake [*Plafker and Savage*, 1970; *Cifuentes*, 1989, Figure 1]. To the North, large slip stops at 34.5°S and from there, slip decreases to reach 0 at 34.2°S. This corresponds to the southern limit of the 1985 central Chile- Vaparaiso earthquake [*Comte et al.*, 1986; *Mendoza et al.*, 1994; *Barrientos*, 1995, Figure 1]. The 2010 earthquake ruptured the seismic gap studied by *Campos et al.* [2002], but it extended further to the north.

[23] We retrieved the main properties of the 2010 central Chile earthquake rupture from the joint inversion of geodetic and seismological data. Among these data, High Rate GPS time series were used as if they were strong-motion records in the frequency domain below 1 Hz, providing ground displacement seismograms free of integration biases. Equipping potential rupture zones with High Rate GPS stations may provide a wealth of high quality data to constrain future earthquake source inversions.

[24] **Acknowledgments.** We are grateful to individuals and institutions operating CGPS stations in Chile and Argentine and contributing to the IGS (JPL, BKG, SHOA, G2, CERI). We deeply thank the Instituto Geográfico Nacional (IGN) from Argentine for making their data publicly available through the RAMSAC CGPS network (http://www.ign.gob.ar/ramsac). We thank the IRIS data center for providing easy access to worldwide broadband waveforms. We are grateful to the NIED Institute of Japan and Geo (http://supersites.unavco.org/main.php) for making the InSAR data publicly available.

References

Altamimi, Z., X. Collilieux, J. Legrand, B. Garayt, and C. Boucher (2007), ITRF2005: A new release of the International Terrestrial Reference Frame based on time series of station positions and Earth Orientation Parameters, *J. Geophys. Res.*, *112*, B09401, doi:10.1029/2007JB004949.

Barrientos, S. (1995), Dual seismogenic behaviour: The 1985 central Chile earthquake, *Geophys. Res. Lett.*, *22*, 3541–3544, doi:10.1029/95GL03316.

Bouchon, M. (1981), A simple method to calculate Green's functions for elastic layered Media, *Bull. Seismol. Soc. Am.*, *71*, 959–971.

Campos, J., D. Hatzfeld, R. Madariaga, G. Lopez, E. Kausel, A. Zollo, S. Barrientos, and H. Lyon-Caen (2002), The 1835 seismic gap in south central Chile, *Phys. Earth Planet. Inter.*, *132*, 177–195, doi:10.1016/S0031-9201(02)00051-1.

Choi, K., A. Bilich, K. M. Larson, and P. Axelrad (2004), Modified sidereal filtering: Implications for high-rate GPS positioning, *Geophys. Res. Lett.*, *31*, L22608, doi:10.1029/2004GL021621.

Cifuentes, I. L. (1989), The 1960 Chilean earthquakes, *J. Geophys. Res.*, *94*, 665–680, doi:10.1029/JB094iB01p00665.

Comte, D., A. Eisenberg, E. Lorca, M. Pardo, L. Ponce, R. Saragoni, S. K. Sing, and G. Suárez (1986), The central Chile earthquake of 3 March 1985: A repeat of previous great earthquakes in the region?, *Science*, *233*, 449–453, doi:10.1126/science.233.4762.449.

Delouis, B., et al. (1997), The Mw = 8:0 Antofagasta (northern Chile) earthquake of 30 July, 1995: A precursor to the end of the large 1877 gap, *Bull. Seismol. Soc. Am.*, *87*, 427–445.

Delouis, B., D. Giardini, P. Lundgren, and J. Salichon (2002), Joint inversion of InSAR, GPS, teleseismic and strong motion data for the spatial and temporal distribution of earthquake slip: Application to the 1999 Izmit mainshock, *Bull. Seismol. Soc. Am.*, *92*, 278–299, doi:10.1785/0120000806.

Delouis, B., M. Pardo, D. Legrand, and T. Monfret (2009), The Mw 7.7 Tocopilla earthquake of 14 November 2007 at the southern edge of the northern Chile seismic Gap: Rupture in the deep part of the coupled plate interface, *Bull. Seismol. Soc. Am.*, *99*, 87–94, doi:10.1785/0120080192.

Dow, J. M., R. E. Neilan, and C. Rizos (2009), The International GNSS Service in a changing landscape of Global Navigation Satellite Systems, *J. Geod.*, *83*, 191–198, doi:10.1007/s00190-008-0300-3.

Hartzell, S. (1978), Earthquake aftershocks as Green's functions, *Geophys. Res. Lett.*, *5*, 1–4, doi:10.1029/GL005i001p00001.

Herring, T. A., R. W. King, and S. C. McClusky (2009), *Documentation of the MIT GPS Analysis Software: GAMIT v 10.35*, Mass. Inst. of Technol., Cambridge.

Madariaga, R., C. Vigny, M. Métois, and J. Campos (2010), Central Chile finally breaks, *Science*, *328*, 181–182, doi:10.1126/science.1189197.

Mendoza, C., S. Hartzell, and T. Monfret (1994), Wide-band analysis of the 3 March 1985 central Chile earthquake: Overall source process and rupture history, *Bull. Seismol. Soc. Am.*, *84*, 269–283.

Nabelek, J. (1984), Determination of earthquake fault parameters from inversion of body waves, Ph.D. thesis, 361 pp., Mass. Inst. of Technol., Cambridge.

Ozawa, T. (2010), Utilization of ALOS-2 for crustal deformation detection of earthquake and volcano, paper presented at ALOS-2 symposium, Jpn. Aerosp. Explor. Agency, Tokyo, 26 March.

Plafker, G., and J. C. Savage (1970), Mechanism of the Chilean earthquake of May 21 and 22, 1960, *Geol. Soc. Am. Bull.*, *81*, 1001–1030, doi:10.1130/001607606(1970)81[1001:MOTCEO]2.0.CO;2.

Pritchard, M. E., and M. Simons (2006), An aseismic slip pulse in northern Chile and along-strike variations in seismogenic behavior, *J. Geophys. Res.*, *111*, B08405, doi:10.1029/2006JB004258.

Ruegg, J. C., A. Rudloff, C. Vigny, R. Madariaga, J. B. de Chabalier, J. Campos, E. Kausel, S. Barrientos, and D. Dimitrov (2009), Interseismic strain accumulation measured by GPS in the seismic gap between Constitución and Concepción in Chile, *Phys. Earth Planet. Inter.*, *175*, 78–85, doi:10.1016/j.pepi.2008.02.015.

Savage, J. C. (1980), Dislocations in seismology, in *Dislocations in Solids*, edited by F. R. N. Navarro, pp. 252–339, North-Holland, New York.

Schwartz, S. Y. (1999), Noncharacteristic behavior and complex recurrence of large subduction zone earthquakes, *J. Geophys. Res.*, *104*, 23,111–23,125, doi:10.1029/1999JB900226.

Vallée, M. (2004), Stabilizing the empirical Green function analysis: Development of the projected Landweber method, *Bull. Seismol. Soc. Am.*, *94*, 394–409, doi:10.1785/0120030017.

B. Delouis, J.-M. Nocquet, and M. Vallée, Geoazur, Observatoire de la Côte d'Azur, Université de Nice – Sophia Antipolis, CNRS, IRD, 250 rue A. Einstein, F-06560 Valbonne, France.